




RESEARCH ARTICLE

Diffusion-tensor-imaging 1-year-old and 2-year-old infant brain atlases with comprehensive gray and white matter labels

Limei Song^{1,2,3} | Yun Peng⁴  | Minhui Ouyang^{2,5}  | Qinmu Peng² |
Lei Feng^{1,2} | Susan Sotardi² | Qinlin Yu² | Huiying Kang⁴ |
Kay L. Sindabizera² | Shuwei Liu¹ | Hao Huang^{2,5} 

¹Research Center for Sectional and Imaging Anatomy, Shandong University School of Medicine, Jinan, Shandong, China

²Department of Radiology, Children's Hospital of Philadelphia, Philadelphia, Pennsylvania, USA

³School of Medical Imaging, Weifang Medical University, Weifang, China

⁴Department of Radiology, Beijing Children's Hospital, Capital Medical University, Beijing, China

⁵Department of Radiology, Perelman School of Medicine, University of Pennsylvania, Philadelphia, Pennsylvania, USA

Correspondence

Hao Huang, Department of Radiology, Children's Hospital of Philadelphia, University of Pennsylvania, 3401 Civic Center Blvd, Philadelphia, PA 19104, USA.
Email: huangh6@chop.edu

Yun Peng, Department of Radiology, Beijing Children's Hospital, Capital Medical University, No.56, Nanlishi Road, Xicheng District, Beijing 100045, China.
Email: ppengyun@hotmail.com

Shuwei Liu, Research Center for Sectional and Imaging Anatomy, Shandong University School of Medicine, No.44 West Wenhua Road, Jinan, Shandong, 250012, China.
Email: liusw@sdu.edu.cn

Funding information

National Institutes of Health (NIH), Grant/Award Numbers: P50HD105354, R01EB031284, R01MH092535, R01MH125333, R01MH129981, R21MH123930, UM1MH130991; Natural Science Foundation of China, Grant/Award Numbers: 31571237, 81671651; Natural Science Foundation of Shandong Province, Grant/Award Number: ZR2020QH048

Abstract

Human infancy is marked by fastest postnatal brain structural changes. It also coincides with the onset of many neurodevelopmental disorders. Atlas-based automated structure labeling has been widely used for analyzing various neuroimaging data. However, the relatively large and nonlinear neuroanatomical differences between infant and adult brains can lead to significant offsets of the labeled structures in infant brains when adult brain atlas is used. Age-specific 1- and 2-year-old brain atlases covering all major gray and white matter (GM and WM) structures with diffusion tensor imaging (DTI) and structural MRI are critical for precision medicine for infant population yet have not been established. In this study, high-quality DTI and structural MRI data were obtained from 50 healthy children to build up three-dimensional age-specific 1- and 2-year-old brain templates and atlases. Age-specific templates include a single-subject template as well as two population-averaged templates from linear and nonlinear transformation, respectively. Each age-specific atlas consists of 124 comprehensively labeled major GM and WM structures, including 52 cerebral cortical, 10 deep GM, 40 WM, and 22 brainstem and cerebellar structures. When combined with appropriate registration methods, the established atlases can be used for highly accurate automatic labeling of any given infant brain MRI. We demonstrated that one can automatically and effectively delineate deep WM microstructural development from 3 to 38 months by using these age-specific atlases. These established 1- and 2-year-old infant brain DTI atlases can advance our understanding of typical brain development and serve as clinical anatomical references for brain disorders during infancy.

This is an open access article under the terms of the [Creative Commons Attribution-NonCommercial-NoDerivs](https://creativecommons.org/licenses/by-nc-nd/4.0/) License, which permits use and distribution in any medium, provided the original work is properly cited, the use is non-commercial and no modifications or adaptations are made.

© 2024 The Authors. *Human Brain Mapping* published by Wiley Periodicals LLC.

KEYWORDS

atlas, brain mapping, DTI, infant brain, parcellation, template

1 | INTRODUCTION

Human infancy is marked by fastest postnatal brain structural changes across the lifespan. During this period, the brain size dramatically increases to 80–90% of the adult brain volume (Pfefferbaum et al., 1994), mainly resulting from gray matter (GM) expansion (e.g., Gilmore et al., 2012; Huppi et al., 1998; Matsuzawa et al., 2001) and white matter (WM) myelination (e.g., Ouyang et al., 2019; Yakovlev & Lecours, 1967). These neuroanatomical changes lay the foundation for establishing complex cerebral circuits that support various brain functions (e.g., Herschkowitz, 2000; Ouyang et al., 2020). Importantly, deviations in these developmental changes have been associated with neurodevelopmental disorders such as autism (e.g., Courchesne & Pierce, 2005; Hazlett et al., 2017; Ouyang et al., 2016). Therefore, understanding brain development during this period is of great interest, and brain atlases play a crucial role as a prerequisite to tracking maturational changes. Specifically, brain atlases provide a reference for reporting the anatomic location of regions of interest (ROIs) and enabling ROI-based quantification of brain properties (Oishi et al., 2008; Toga et al., 2006), as well as enhancing the comparability of intersubject and inter-study comparison. However, using adult templates and atlases for infant brains can lead to significant offsets of the labeled structures due to large differences in global and regional brain sizes and shapes, as well as signal intensity profiles in brain images between these two populations. Age-specific atlases are urgently needed for precision medicine to improve the accuracy of pediatric brain normalization and segmentation (e.g., Feng et al., 2019; Huang et al., 2019; Huang, 2022; Matsuzawa et al., 2001; Oishi et al., 2019; Richards & Xie, 2015; Wilke et al., 2003), particularly for the first 2 years of life.

Atlas-based automated labeling is a more effective and efficient way to study brain morphology and parcellate the brain for subsequent analyses, compared with time-consuming manual labeling. While brain atlases are relatively well established for adults (e.g., Collins et al., 1994; Desikan et al., 2006; Fan et al., 2016; Mori et al., 2008; Oishi et al., 2008) and neonates (e.g., Alexander et al., 2017; de Macedo Rodrigues et al., 2015; Feng et al., 2019; Gousias et al., 2012; Kabdebon et al., 2014; Oishi et al., 2011), they are not fully developed for young children aged 1 and 2 years. Although several infant brain atlases have emerged (de Macedo Rodrigues et al., 2015; Gousias et al., 2008; Shi et al., 2011; Yoshida et al., 2013) due to advances in computing and medical imaging technologies, these atlases are mainly confined to GM structures and do not include essential WM structures that connect different brain regions. Moreover, these infant atlases were often created using adult atlases based on conventional T1-weighted (T1w) or T2-weighted (T2w) images and do not properly account for anatomical shape and

tissue contrast differences between these two populations (e.g., Gousias et al., 2008; Shi et al., 2011).

Comprehensive anatomical delineation of human infant brain solely based on conventional T1w and T2w structural MRI is challenging. The contrast changes of T1w and T2w MRI are prominent throughout the first 2 years of life due to myelination (Barkovich, 2000; Huang, 2022; Ouyang et al., 2019). The contrasts of T1w or T2w MRI cannot be used to delineate different WM structures. The maps derived from diffusion tensor imaging (DTI) (Basser et al., 1994), on the other hand, offer relatively stable and high contrasts throughout 0–2 years of age (Feng et al., 2019; Huang, 2022; Oishi et al., 2019; Ouyang et al., 2019). DTI-derived maps especially provide higher contrasts in the WM regions of infant brain. For instance, WM tracts such as the internal capsule are barely visible on conventional T1w and T2w images of the infant brain, whereas DTI orientation-encoded colormap enables clear visualization of these structures. Multiple contrasts from DTI-derived maps, including fractional anisotropy (FA), axial, radial and mean diffusivity (MD), offer rich information of brain tissues that can guide the delineation of immature WM structures more precisely than conventional T1w or T2w MRI. Thus, DTI is a uniquely suitable for delineating various neuroanatomical structures of infant brain (e.g., Feng et al., 2019; Huang et al., 2006; Oishi et al., 2019). DTI atlases are available for adult and neonate brains. However, to date, no comprehensive DTI atlas is available for infants. Given already established DTI atlases (e.g., Feng et al., 2019; Oishi et al., 2011) for neonates representing beginning time point of the infancy, 1- and 2-year of age were selected as two time points for establishing age-specific infant brain atlases in this study as they represent landmark infant developmental time points at middle and end of infancy, respectively. Age-specific DTI atlases with rich anatomical labeling covering both GM and WM structures fill knowledge gap of lacking DTI atlases of these critical ages, provide clinical references and serve as fundamental anatomical backbone for understanding brain maturation in health and disorders during this dynamic developmental phase.

In this study, we aimed to create age-specific brain DTI templates and atlases for the 1- and 2-year-old age groups. T1w and DTI images of 50 typically developing (TD) children were obtained to create these brain templates and atlases. The templates include single-subject, as well as linear and nonlinear population-averaged templates. Each age-specific three-dimensional (3D) digital infant brain atlas includes comprehensive 124 GM and WM labels, which appear smooth in all axial, coronal, and sagittal planes, demonstrating quality of the atlas labels. All presented atlases and templates are disseminated through the public website brainmrimap.org. We further examined the reliability and accuracy of automated labeling using the established atlases. Application of using these age-specific DTI atlases to study WM tract

microstructural maturation from birth to 3 years old was demonstrated.

2 | MATERIALS AND METHODS

2.1 | Participants

A total of 90 TD subjects aged from 3 to 38 months (18.53 ± 8.50 months) were recruited from Beijing Children's Hospital to participate in this study. Among these 90 subjects, 23 infants with postnatal age 9.47–14.93 months (12.67 ± 2.21 months) and 27 toddlers with postnatal age of 20.03–27.73 months (23.13 ± 2.48 months) were used to construct the 1-year-old and 2-years-old templates, respectively. All participants had normal neurological examinations documented in their medical record. They were referred for MRI for non-neurological reasons including seizures with fever, intermittent headache, sexual precocity, short stature, or convulsion. The exclusion criteria for participants included known nervous system disease, history of psychiatric, neurodevelopmental or systemic illness. The clinical history of each child in this TD cohort was carefully inspected by pediatric radiologists (H.K. and Y.P.) to rule out developmental abnormalities. This study was approved by Beijing Children's Hospital Research Ethics Committee (Approval number 2016-36), and written informed consent was obtained from each child's parents.

2.2 | Diffusion and T1-weighted MRI data acquisition

All participants were scanned on a 3T Philips Achieva system (Philips Healthcare, Best, The Netherlands) under sedation. Eight-channel head coil was used. Earplugs and headphones were used to minimize noise exposure. Diffusion MRI (dMRI) was acquired using a single-shot EPI sequence with sensitivity encoding parallel imaging scheme (SENSE, reduction factor = 2). The imaging matrix size was 128×128 with a field of view (FOV) of 256×256 mm². Axial slices with 2 mm thickness were acquired parallel to the anterior–posterior commissure (AC–PC) line. A total of 70 slices covered the entire brain without a slice gap. The repetition time (TR) and echo time (TE) were 9.3 s and 100 ms, respectively. Diffusion weighting was encoded along 30 independent directions, and the *b*-value was 1000 s/mm². To improve the signal-to-noise ratio, two repetitions were performed. The acquisition time of two repetitions of dMRI scans was 11.5 min. T1-weighted (T1w) images of all participants were also acquired using Magnetization Prepared RAPid Gradient Echo sequence with the following parameters: TR = 8.28 ms, TE = 3.82 ms, flip angle = 12°, 150 slices, FOV = 200×200 mm², matrix size = 200×200 , and voxel size = $1 \times 1 \times 1$ mm³. The acquisition time of the T1w image was 3.7 min. Visual inspection was carefully conducted for all MRI data by experienced pediatric radiologists (H.K. and Y.P.) with decades of experience in clinical radiology. No apparent motion artifacts were spotted with the sedated MRI scans.

2.3 | MRI data preprocessing and dMRI-T1w image registration

dMRI data preprocessing included eddy current and motion correction, tensor fitting and estimation of DTI-derived measures was conducted using DTIStudio (Jiang et al., 2006). Specifically, eddy current distortion and head motion were corrected by registering all raw diffusion weighted images (DWIs) to a b0 image using a 12-parameter (affine) automated image registration algorithm (Woods et al., 1998). Whole-brain maps of FA, MD, axial diffusivity (AD), and radial diffusivity (RD) were obtained for all subjects after tensor fitting. DTI orientation-encoded colormaps indicating fiber orientation were also obtained with red (R), green (G), and blue (B) colors assigned to left–right, anterior–posterior, and superior–inferior orientations, respectively. In order to establish the templates and atlases, all T1w and DTI-derived images were first preprocessed with brain extraction and volume resampling procedures. Briefly, FSL's bet tool (fsl.fmrib.ox.ac.uk) was used for skull stripping. *DiffeoMap*'s “Resample Image” tool (mrstudio.org) was used to resample all skull-stripped MRI images to a matrix dimension of $180 \times 220 \times 180$ with a physical resolution of $1 \times 1 \times 1$ mm³. To obtain the co-registered T1w and DTI images of each subject, affine and large deformation diffeomorphic metric mapping (LDDMM) transformations (Miller et al., 2002) were used to warp the b0 images to the contrast reversed T1w images. For tensor transformation, the affine and LDDMM transformation matrices obtained from the above procedures were then applied to the diffusion tensor to create normalized tensor fields (Xu et al., 2003) in *DiffeoMap* software. After these procedures, the co-registered T1w and DTI images were created with a 1 mm isotropic resolution.

2.4 | Establishment of population-averaged and single-subject templates

For each specific age of 1- and 2-years-old, two population-averaged templates and a single-subject template were established. The two population-averaged templates included a population-averaged-linear (from linear transformation) and a population-averaged-nonlinear (from nonlinear transformation) template. To generate the age-specific DTI templates, the seven-step procedure used for establishing neonate atlas (Feng et al., 2019; Oishi et al., 2011) was adopted. Briefly, the first step was co-registering T1w and DTI images of each subject, as described in the above section. Second, all co-registered T1w and DTI images then underwent AC–PC alignment to obtain the AC–PC co-registered T1w images (reg-T1w images) and DTI maps (reg-DTI maps), respectively. After registering all reg-T1w images to a representative subject's image using affine transformation, an averaged image was then created in the third step and served as a tentative template (first template) for the next step. Fourth, all reg-T1w images were then normalized to the first template using affine transformation to create another averaged image as a tentative template (second template). Fifth, each reg-T1w image was normalized to the second template using affine transformation to create an averaged

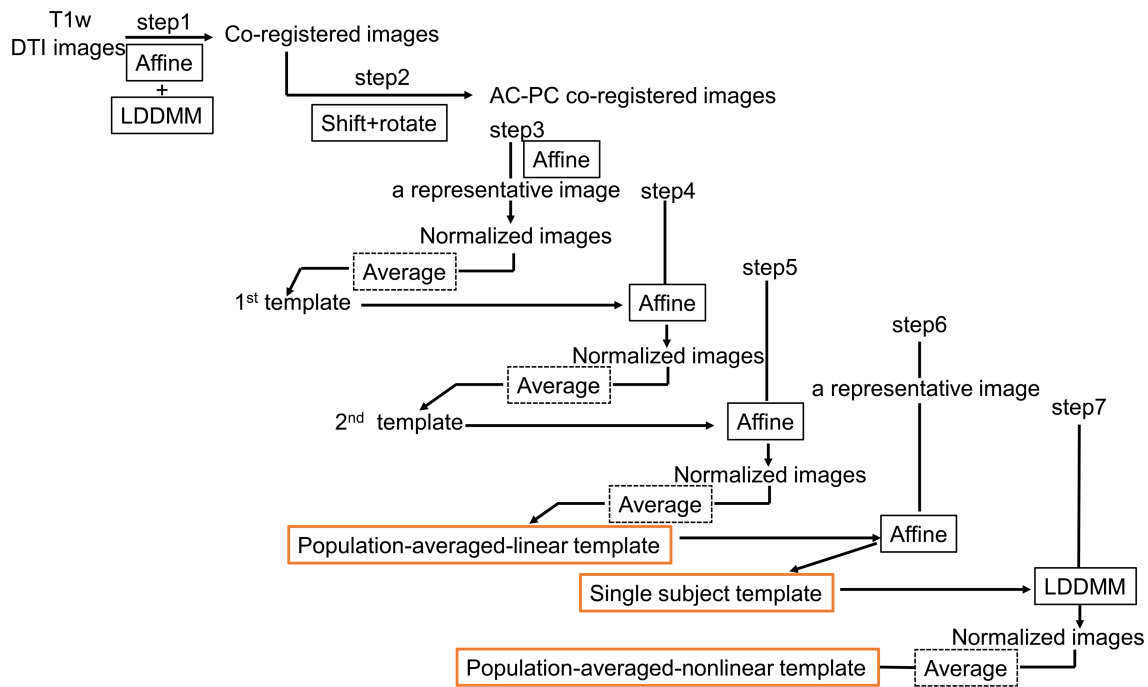


FIGURE 1 The seven-step procedures for building the single subject, population-averaged linear, and population-averaged nonlinear infant template.

image with sharper edges. The linear transformation matrices from the fifth step were then applied to the reg-DTI maps to create averaged DTI-derived maps. This set of averaged T1w and DTI-derived maps worked as the population-averaged-linear template (the outcome of the fifth step). Next, a representative single-subject image was linearly normalized to the population-averaged-linear template to generate the single-subject template as the outcome of the sixth step. Finally, the reg-T1w and reg-DTI maps were nonlinearly normalized to the single-subject template using LDDMM registration, with reg-T1w to drive the transformation. The resultant images were then averaged to create the population-averaged-nonlinear template (the outcome of the seventh step). The affine and LDDMM transformation matrices obtained from the scalar images were applied to the tensor field to create normalized tensor fields. All transformations were performed using *DiffeoMap* software. The workflow of the seven-step procedures for building the templates is shown in Figure 1.

2.5 | Computation of Jacobian determinants

To demonstrate the morphological differences between a 1-year-old subject's brain and the established 1-year-old, 2-year-old, and JHU-DTI-MNI adult (Oishi et al., 2008) templates, the whole brain Jacobian determinant maps were calculated. Here, ten 1-year-old children were randomly selected and registered to the established age-specific 1-year-old, 2-year-old and JHU-DTI-MNI single-subject templates using an LDDMM registration with T1w images to drive the transformations. Ten transformation matrices were then generated from registrations to each template. Based on the generated LDDMM

transformation matrices, logarithms of the Jacobian determinants of the entire brain were computed (Huang et al., 2005). Three averaged maps of Jacobian determinant of the entire brain based on the 10 transformation matrices were calculated: the 1-year-old, 2-year-old and JHU-DTI-MNI single-subject templates (Figure 2a). The histograms of the regional volumetric changes were established with the whole brain Jacobian determinant maps obtained above (Figure 2b).

2.6 | Establishment of the comprehensive GM and WM brain atlases

DTI-derived maps and T1w images offer high contrasts for cerebral cortical gyri, subcortical nuclei and WM tracts and were used for manual delineation of various neural structures. The atlas labeling protocol adopted here is consistent with those used to establish previous adult and neonate human brain atlases (Feng et al., 2019; Mori et al., 2008; Oishi et al., 2008, 2011) as well as adult macaque brain atlas (Feng et al., 2017). Manual annotation and labeling of brain structures were primarily conducted on two-dimensional (2D) axial planes of the single-subject templates at 1- and 2-year-old with *ROIEditor* (mrstudio.org), followed by adjustments in coronal and sagittal planes. Available atlases (Feng et al., 2019; Oishi et al., 2008; Oishi et al., 2011) were used for neuroanatomical guidance. Labels of "all" neural structures were manually adjusted and refined with neuroanatomists' months of manual work. The annotations and labels of all major WM tracts were manually delineated on the DTI orientation-encoded colormaps. WM tracts that are adjacent to the subcortical nuclei, such as external capsule (ec) and

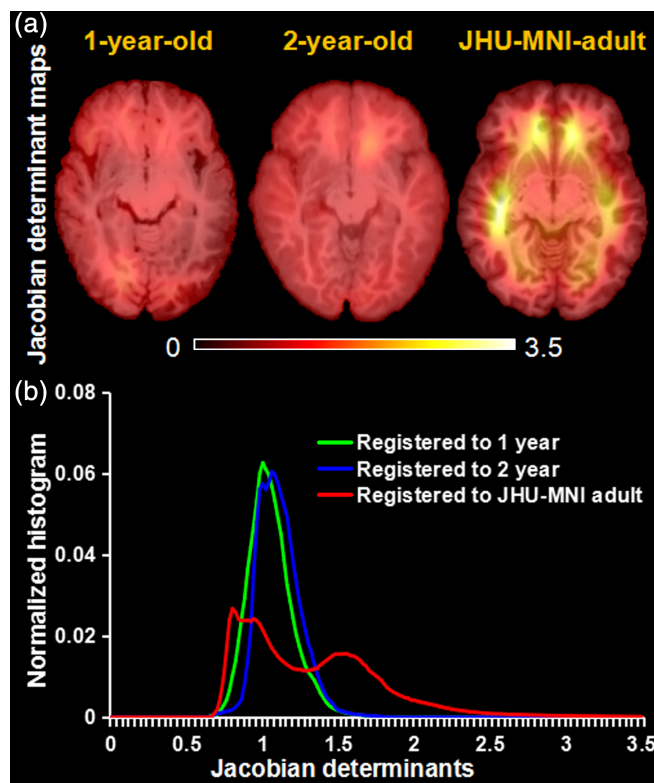


FIGURE 2 Jacobian determinant maps overlaid on the 1-year-old (left panel), 2-year-old (middle panel) and JHU-MNI-adult (right panel) T1w templates in (a) are based on registration of ten 1-year-old randomly selected subject brains to the 1-year-old, 2-year-old, and JHU-MNI-adult single-subject template using nonlinear registration. Normalized Jacobian determinant histogram showing distribution of the Jacobian determinant values with transformations from these ten 1-year-old subject brains to the 1-year-old (green), 2-year-old (blue), and JHU-MNI-adult (red) template is shown in (b).

anterior limb, posterior limb and retrolenticular part of internal capsule (alic, plic, and rlic), were delineated with the contrasts of DTI orientation-encoded colormaps as well as FA maps and averaged DWI (aDWI) images. All major GM structures, including the cerebral cortex and subcortical nuclei, were delineated on the T1w images. The sulcal and gyral patterns from T1w images facilitate the labeling of cerebral cortical structures. Extensive manual delineation on the 2D planes of one view (e.g., axial) followed by adjustments in the 2D planes of the other two views (e.g., coronal and sagittal) of the DTI-derived maps or T1w images were repeated until the boundaries of each labeled neural structure of all three views (axial, coronal, and sagittal) became smooth. To achieve accurate labeling, the WM tracts were three-dimensionally reconstructed by DTI tractography (Mori et al., 1999) for accurately identify the location and boundary. Similarly, the cerebral cortex and subcortical nuclei were also 3D reconstructed using Amira Software (FEI software, Hillsboro, OR), so that cross-sectional boundaries of the 3D reconstructed parcellated cortical gyral surfaces and subcortical nuclei were used to refine the labeling. A total of 124 comprehensively

labeled GM and WM structures were then delineated and annotated for 1- and 2-year-old children's brains, as shown in Table 1. The above-mentioned procedures have been used to establish the comprehensive macaque (Feng et al., 2017) and human neonate atlases (Feng et al., 2019) and proved to be effective. All manual adjusting and refining processes for the 1- and 2-year-old atlases were conducted by a neuroanatomist (L.S.) under the guidance of the major contributor (L.F.) of previous established neonate and macaque brain atlases (Feng et al., 2017; Feng et al., 2019). An experienced neuroanatomist (S.L. with more than 35 years of experience) verified the accuracy of final parcellated neural structures in each atlas.

2.7 | Evaluation of the age-specific atlases for automated labeling

To test the accuracy of automated labeling using established age-specific atlases, datasets of 5 subjects in 1-year-old and 2-year-old groups (in total 10 subjects) were randomly selected, excluding the ones used for establishing single-subject templates. The reliability and misclassification error were validated by Dice ratio and L1 error, respectively. For each subject, 10 representative brain structures on five consecutive 2D image slices were selected for quantitative evaluation. These 10 brain structures included six WM tracts, two subcortical GM, and two cortical gyri. These brain structures were delineated manually (manual delineation) on the predetermined 2D image slices in the native space by two raters (L.F. and L.S.) to investigate inter-rater variability. The delineation protocol is identical to the one used for labeling the atlases. Automated labeling of the neural structures was obtained by transforming the atlas parcellation maps to each subject's native space images using affine and LDDMM transformations. The registered parcellation maps were overlaid onto each subject's images to segment the brain structures automatically.

Dice ratio and L1 error were used to evaluate the overlap and misclassification of two delineations (manual vs. automated delineations, and manual vs. manual delineations). The manual and automated delineations of each structure were saved as binary maps. The two binary maps of each brain structure were overlaid. All voxels could be categorized into the following three groups: (1) voxels that were outside the structure in either delineation (nn); (2) voxels that were inside in only one of these two delineations (pn, np); (3) voxels that contained the structure in both delineations (pp). After this categorization, the Dice ratio was defined as $2pp/(pn + 2pp + np)$ and L1 error was calculated as $(1 - pp/(pp + pn + np))/2$. The Dice ratio and L1 error measurements within the manual trials by two different raters provided the level of precision for manual delineation, serving as gold standard. To test the accuracy and reliability of the atlas-based automated labeling, the reliability analyses between manual and automated delineations were conducted. Here, the manual delineation results from rater L.S. served as references for measuring the accuracy of automated labeling.

TABLE 1 Neuroanatomical labels of 124 gray and white matter structures and their abbreviations.

	Abbreviation	Structure	Left/right
1	cc	Corpus callosum	Left
2	cc	Corpus callosum	Right
3	alic	Anterior limb of internal capsule	Left
4	alic	Anterior limb of internal capsule	Right
5	plic	Posterior limb of internal capsule	Left
6	plic	Posterior limb of internal capsule	Right
7	rlic	Retrolenticular part of internal capsule	Left
8	rlic	Retrolenticular part of internal capsule	Right
9	acr	Anterior corona radiata	Left
10	acr	Anterior corona radiata	Right
11	scr	Superior corona radiata	Left
12	scr	Superior corona radiata	Right
13	pcr	Posterior corona radiata	Left
14	pcr	Posterior corona radiata	Right
15	cgc	Cingulum cingulate gyrus part	Left
16	cgc	Cingulum cingulate gyrus part	Right
17	cgh	Cingulum hippocampal part	Left
18	cgh	Cingulum hippocampal part	Right
19	fx	Fornix	Left
20	fx	Fornix	Right
21	st	Stria terminalis	Left
22	st	Stria terminalis	Right
23	tap	Tapetum	Left
24	tap	Tapetum	Right
25	slf	Superior longitudinal fasciculus	Left
26	slf	Superior longitudinal fasciculus	Right
27	ec	External capsule	Left
28	ec	External capsule	Right
29	ptr	Posterior thalamic radiata	Left
30	ptr	Posterior thalamic radiata	Right
31	ss	Sagittal stratum	Left
32	ss	Sagittal stratum	Right
33	Tha	Thalamus	Left
34	Tha	Thalamus	Right
35	Put	Putamen	Left
36	Put	Putamen	Right
37	GP	Globus pallidus	Left
38	GP	Globus pallidus	Right
39	Caud	Caudate	Left
40	Caud	Caudate	Right
41	cp	Cerebral peduncle	Left
42	cp	Cerebral peduncle	Right
43	sfo	Superior fronto-occipital fasciculus	Left
44	sfo	Superior fronto-occipital fasciculus	Right
45	ifo	Inferior fronto-occipital fasciculus	Left
46	ifo	Inferior fronto-occipital fasciculus	Right

TABLE 1 (Continued)

	Abbreviation	Structure	Left/right
47	cst	Corticospinal tract	Left
48	cst	Corticospinal tract	Right
49	scp	Superior cerebellar peduncle	Left
50	scp	Superior cerebellar peduncle	Right
51	mcp	Middle cerebellar peduncle	Left
52	mcp	Middle cerebellar peduncle	Right
53	icp	Inferior cerebellar peduncle	Left
54	icp	Inferior cerebellar peduncle	Right
55	pct	Pontine crossing tract	Left
56	pct	Pontine crossing tract	Right
57	unc	Uncinate fasciculus	Left
58	unc	Uncinate fasciculus	Right
59	midbrain	Midbrain	Left
60	midbrain	Midbrain	Right
61	pons	Pons	Left
62	pons	Pons	Right
63	ml	Medial lemniscus	Left
64	ml	Medial lemniscus	Right
65	medulla	Medulla oblongata	Left
66	medulla	Medulla oblongata	Right
67	SFG	Superior frontal gyrus	Left
68	SFG	Superior frontal gyrus	Right
69	MFG	Middle frontal gyrus	Left
70	MFG	Middle frontal gyrus	Right
71	IFG	Inferior frontal gyrus	Left
72	IFG	Inferior frontal gyrus	Right
73	MFOG	Medial fronto-orbital gyrus	Left
74	MFOG	Medial fronto-orbital gyrus	Right
75	LFOG	Lateral fronto-orbital gyrus	Left
76	LFOG	Lateral fronto-orbital gyrus	Right
77	RG	Gyrus rectus	Left
78	RG	Gyrus rectus	Right
79	PrCG	Precentral gyrus	Left
80	PrCG	Precentral gyrus	Right
81	PoCG	Postcentral gyrus	Left
82	PoCG	Postcentral gyrus	Right
83	SPL	Superior parietal gyrus	Left
84	SPL	Superior parietal gyrus	Right
85	PrCu	Precuneus	Left
86	PrCu	Precuneus	Right
87	CingG	Cingulate gyrus	Left
88	CingG	Cingulate gyrus	Right
89	SMG	Supramarginal gyrus	Left
90	SMG	Supramarginal gyrus	Right
91	AG	Angular gyrus	Left
92	AG	Angular gyrus	Right

(Continues)

TABLE 1 (Continued)

	Abbreviation	Structure	Left/right
93	STG	Superior temporal gyrus	Left
94	STG	Superior temporal gyrus	Right
95	MTG	Middle temporal gyrus	Left
96	MTG	Middle temporal gyrus	Right
97	ITG	Inferior temporal gyrus	Left
98	ITG	Inferior temporal gyrus	Right
99	FuG	Fusiform gyrus	Left
100	FuG	Fusiform gyrus	Right
101	PHG	Parahippocampal gyrus	Left
102	PHG	Parahippocampal gyrus	Right
103	ENT	Entorhinal gyrus	Left
104	ENT	Entorhinal gyrus	Right
105	SOG	Superior occipital gyrus	Left
106	SOG	Superior occipital gyrus	Right
107	MOG	Middle occipital gyrus	Left
108	MOG	Middle occipital gyrus	Right
109	IOG	Inferior occipital gyrus	Left
110	IOG	Inferior occipital gyrus	Right
111	Cu	Cuneus	Left
112	Cu	Cuneus	Right
113	LG	Lingual gyrus	Left
114	LG	Lingual gyrus	Right
115	Ins	Insular cortex	Left
116	Ins	Insular cortex	Right
117	Hippo	Hippocampus	Left
118	Hippo	Hippocampus	Right
119	Amyg	Amygdala	Left
120	Amyg	Amygdala	Right
121	Cerebellum	Cerebellar hemisphere	Left
122	Cerebellum	Cerebellar hemisphere	Right
123	ac	Anterior commissure	Left
124	ac	Anterior commissure	Right

2.8 | Measurement of WM tract microstructural changes during development based on automated atlas labels

For illustrating possible application of these established age-specific DTI atlases, we further mapped these atlases to the DTI data of 90 subjects aged from 3 to 38 months (18.53 ± 8.50 months) to explore the WM microstructural development. The 1-year-old brain atlas was used to automatically label DTI data of children aged 3–18 months, whereas the 2-year-old atlas was used to automatically label the DTI data from children aged 18 to 38 months. DTI-derived measurements (FA, MD, AD, and RD) of the major deep WM tracts were then obtained for 90 children using tract-wise ROIs. Briefly, the

atlas parcellation maps were wrapped to the subjects' native space using affine and LDDMM transformation to obtain WM tract-wise ROIs. DTI parameters of these major WM tracts were measured based-on these tract-wise ROIs. The cortical areas and ventricles were omitted. These major deep WM tracts were categorized into five functionally distinctive tract groups, namely limbic, projection, commissural, association, and brainstem tracts (Wakana et al., 2004). Linear fitting of FA, MD, AD, and RD measurements of the following five tracts representing respective five tract groups was conducted to demonstrate heterogeneous microstructural development among WM tract groups: corpus callosum (cc: representing commissural tract group), superior corona radiata (scr: representing projection tract group), fornix (fx: representing limbic tract group), inferior

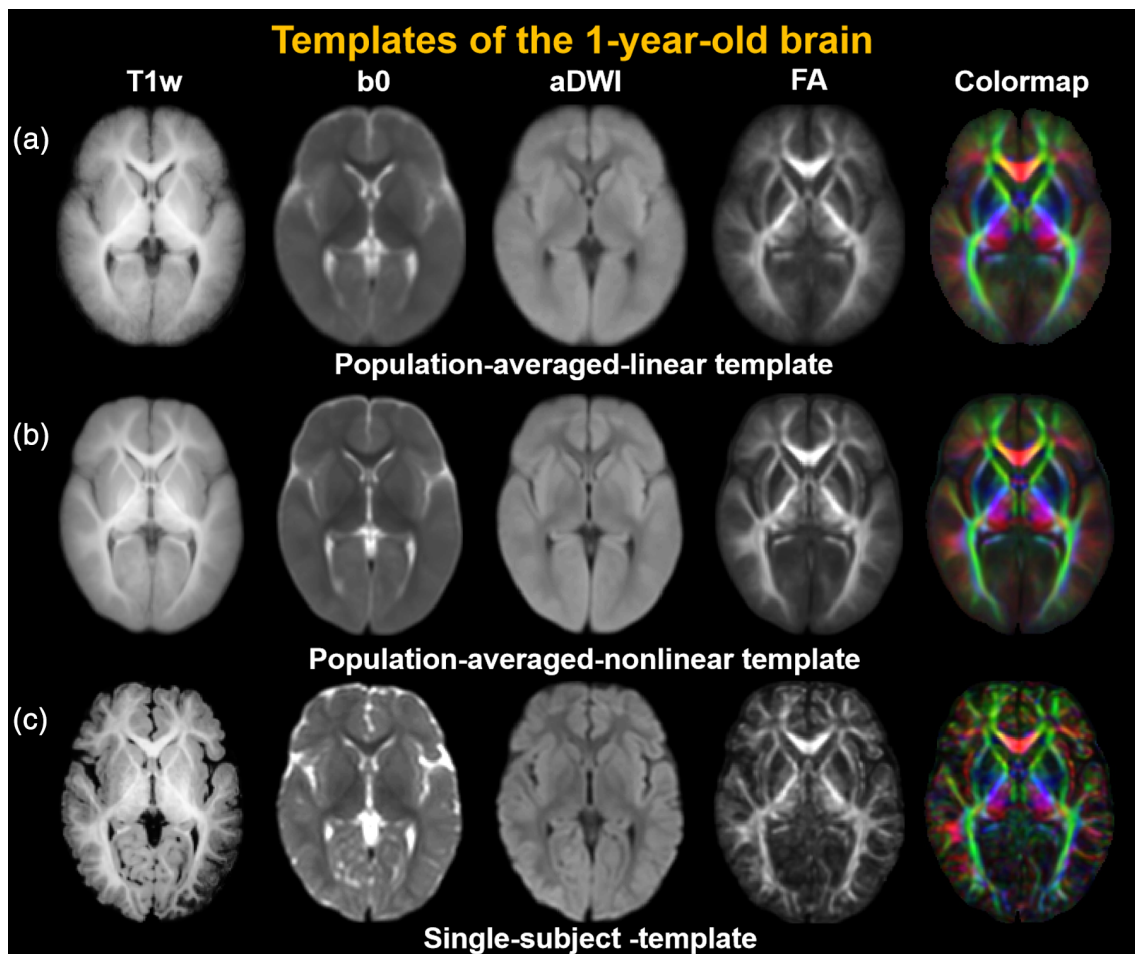


FIGURE 3 Population-averaged-linear (a), population-averaged-nonlinear (b), and single-subject (c) templates for 1-year-old brains. From left to right: T1-weighted (T1w) images, b0 images, averaged diffusion weighted image (aDWI), fractional anisotropy (FA) map, and DTI orientation-encoded colormaps.

fronto-occipital fasciculus (ifo: representing association tract group), and inferior cerebellar peduncle (icp: representing brainstem tract group).

3 | RESULTS

3.1 | Large morphological changes between 1-year-old infant to adult brains

The whole brain morphological changes between a 1-year-old infants' brain images and established 1-year-old, 2-year-old, and adult templates are presented in Figure 2 using Jacobian determinate measurements. Registered 1-year-old infants' brain images using an age-specific infant brain template (i.e., 1-year-old template) are associated with less morphological deformation than registered 1-year-old infants' brain images using an adult brain template. Smaller Jacobian determinants are obtained when the test subject's age is the same as that of the template. A larger age gap between the test subject and the template results in larger absolute Jacobian determinants. Higher

local volume expansions (Jacobian determinant greater than 1) are apparent in frontal and temporal areas from 1-year-old to adult template as shown in the Jacobian determinant maps (Figure 2a). The profiles of local volume changes from 1-year-old subject brains to the 1-year-old, 2-year-old, and adult brain templates are shown in Figure 2b. The Jacobian determinant with the transformation from 1-year-old infant brains to the 1-year-old template is more concentrated, and the center of the Jacobian determinant histogram is close to 1. However, the Jacobian determinant with the transformation from 1-year-old infant brains to the adult brain template is more dispersed, and the center of the Jacobian determinant histogram shifts to around 1.3.

3.2 | Age-specific DTI brain atlases with comprehensive WM and GM neuroanatomical labels

The T1w images, and DTI-derived maps (b0 images, aDWI images, FA maps and orientation-encoded colormaps) of the population-averaged-linear, population-averaged-nonlinear and single-subject

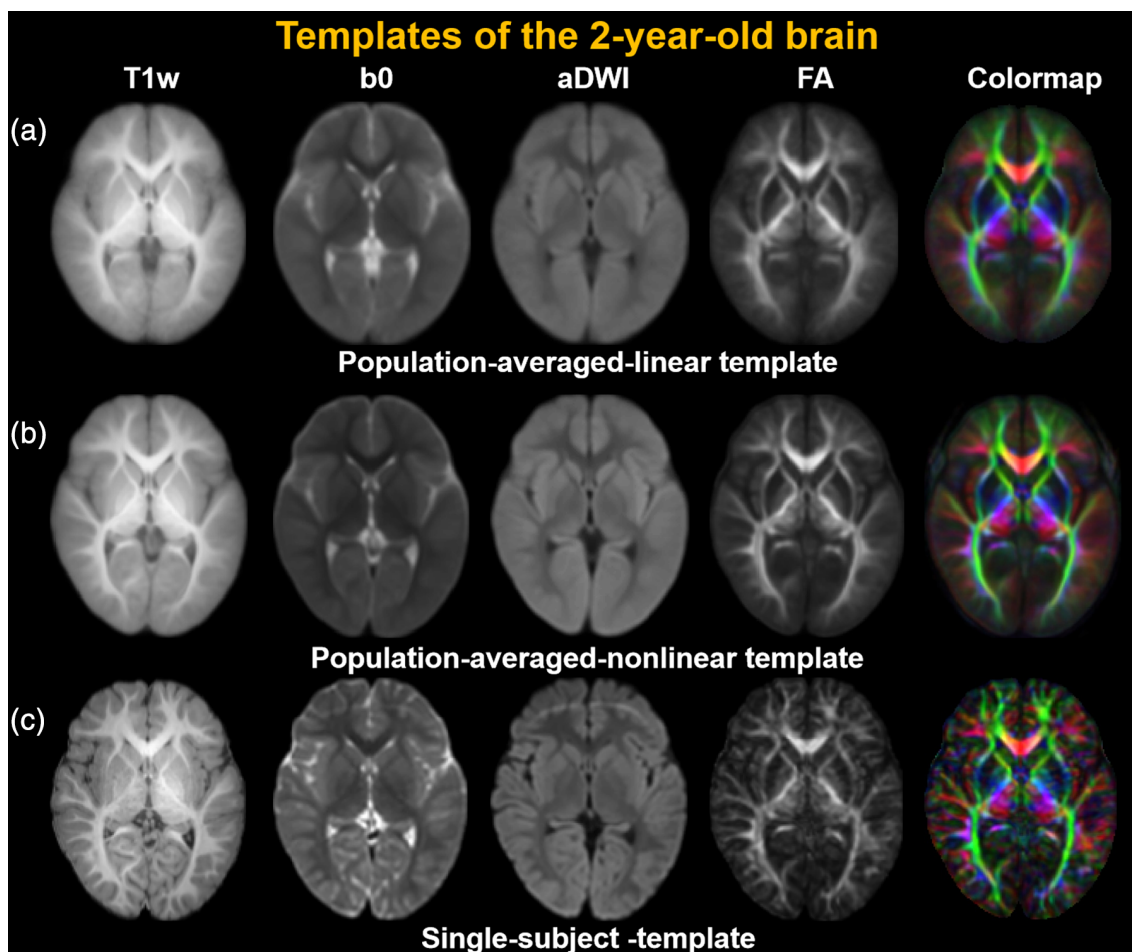


FIGURE 4 Population-averaged-linear (a), population-averaged-nonlinear (b), and single-subject (c) templates for 2-year-old brains. From left to right: T1w images, b0 images, aDWI, FA map, and DTI orientation-encoded colormaps.

templates for 1- and 2-year-old brains are shown in Figures 3 and 4, respectively. Established on the single-subject template images, the atlases display comprehensive labels of 124 WM, cortical, and subcortical neural structures overlaid on high resolution T1w and DTI orientation-encoded colormaps for 1-year-old (Figure 5) and 2-year-old brains (Figure 6). The high degree of alignment between the T1w images and DTI orientation-encoded colormaps can be clearly appreciated in Figures 5 and 6. The labels have been thoroughly refined to ensure the boundaries of all delineated neural structures appear smooth and continuous in all three views. The contours of GM and WM were overlaid onto the T1w images (the left hemisphere) and DTI orientation-encoded colormaps (the right hemisphere) in axial (top panels of Figures 5 and 6) and coronal planes (bottom panels of Figures 5 and 6). The sagittal planes of the atlases were overlaid onto the T1w images (middle panels of Figures 5 and 6). These comprehensive age-specific infant atlases cover 22 brainstem and cerebellar structures, 40 deep WM structures, 10 deep GM structures, and 52 cerebral cortical structures. The indices and abbreviations of all 124 anatomical labels of brain neural structures are listed in Table 1. To demonstrate the neuroanatomical differences between the ages, the age-specific labels are displayed side by side in one figure in the axial, coronal and sagittal planes in the Supplemental Figures 1-3,

respectively. The enlarged regions in these supplemental figures show further details of the parcellated neural structures. The underlying images on the left and right sides of each panel in the Supplemental Figures 1 and 2 are the T1w and DTI orientation-encoded colormaps, respectively. In the Supplemental Figure 3, the underlying images are the T1w maps in the first and third rows and DTI orientation-encoded colormaps maps in the second and fourth rows. Furthermore, the lateral, superior and inferior views of the 3D reconstructed labeled brain structure of cerebral cortex deep WM tracts, and subcortical GM are displayed in Figure 7 for both the 1- and 2-year-old infant brain atlases. It is evident that both GM and WM labels match their corresponding anatomical structures, and the boundaries of all delineated neural structures in these atlases appear smooth in the 3D reconstructed illustrations.

3.3 | Quantitative evaluation for automated labeling

The measurements of Dice ratio and L1 error in Figure 8 demonstrate the potential of these established age-specific atlases for high-accuracy automated labeling of infant brains. The Dice ratio of

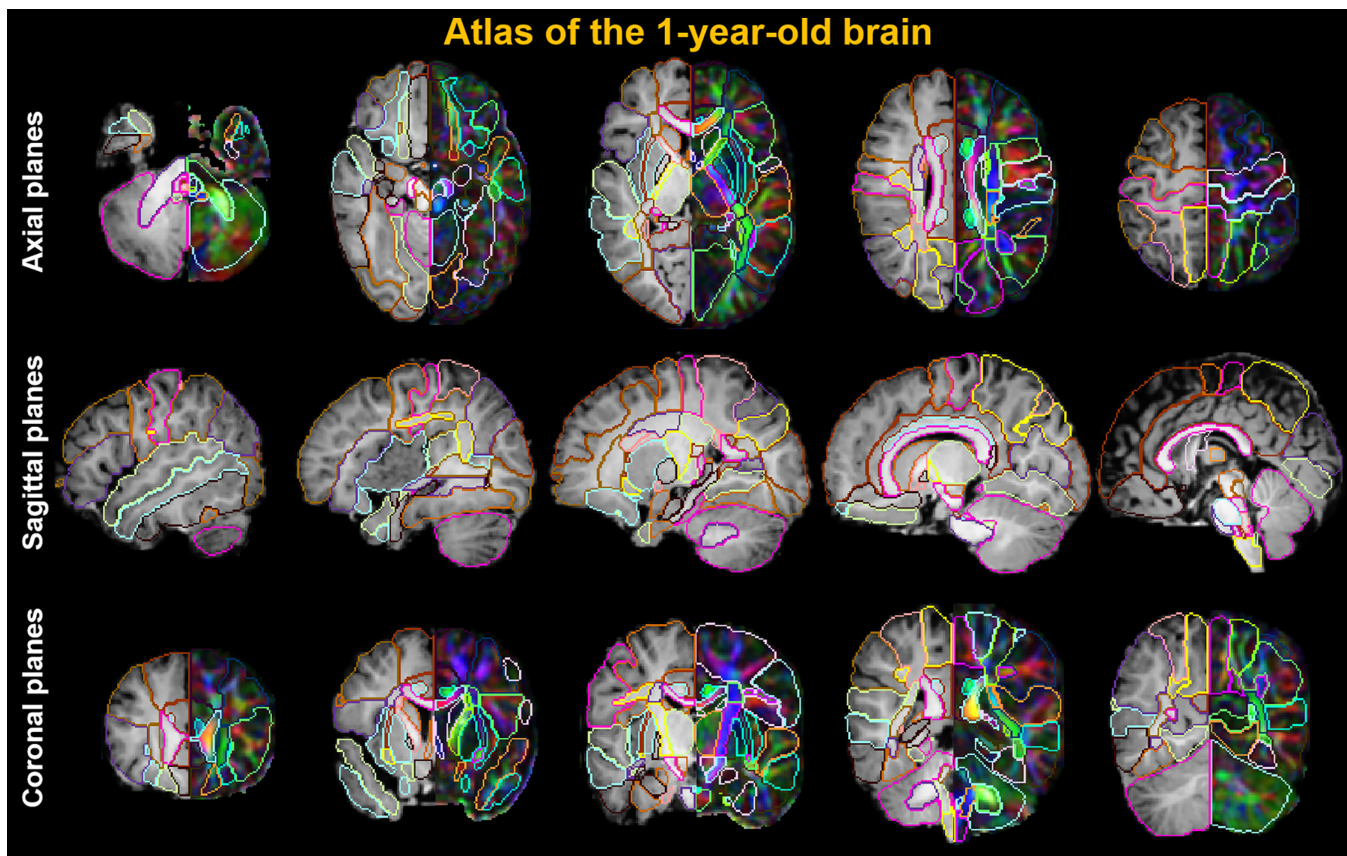


FIGURE 5 Axial, sagittal, and coronal planes of the established 1-year-old brain atlas with comprehensive gray matter (GM) and white matter (WM) labels. Atlas labels are overlaid onto the T1w images (the left hemisphere) and DTI orientation-encoded color maps (the right hemisphere) in axial and coronal planes. Atlas labels are overlaid onto the T1w images in sagittal planes.

manual-manual delineation (inter-rater variability) was higher than 0.8 in most regions, serving as a gold standard. The Dice ratio of both manual delineation and 1- or 2-year-old atlas-based automated labeling was over 0.8 in most regions indicating almost perfect atlas-based automated labeling, with manual delineation as a reference. The Dice ratio was more than 0.75 in cingulum bundle, indicating registration accuracy even for the irregular shape structures. Smaller or comparable standard deviations represented by the Dice ratio error bars of automated labeling indicate high reproducibility. Misclassification of 1- or 2-year-old atlas-based automated labeling by L1 error is as low as that of inter-rater comparison. Therefore, the age-matched 1- and 2-year-old infant atlases could be used for accurate labeling of age-matched brain MRI images automatically and accurately.

3.4 | Microstructural changes of WM tracts from 3 to 38 months

To demonstrate potential applications of using the established age-specific 1- and 2-year-old DTI atlases, the FA, MD, AD, and RD of the deep WM tracts in the 90 children's brains from birth to 3 years of age were measured to reveal the WM microstructural development of the selected tracts. 1- and 2-year-old parcellation maps were

overlaid onto FA images in native space from two representative children (Figure 9a). The age-related changes of five tracts, representing the five tract groups, respectively, are displayed in Figure 9b. We found a general age-related increase of FA and a decrease of MD, AD, and RD in all tested WM tracts ($p < .05$). In addition, these WM tracts show heterogeneous time-dependent changes of FA, MD, AD, and RD, indicating heterogeneous microstructural maturation. Notably, the FA values of the corpus callosum (cc) representing the commissural tract group are remarkably higher than those of other fibers representing the projection, limbic, association and brainstem tract groups as shown in the Supplemental Table 1.

4 | DISCUSSION

In this study, we established 1- and 2-year-old human infant brain DTI atlases, covering 124 comprehensive labels including 52 cerebral cortical, 10 deep GM, 40 deep WM, and 22 brainstem and cerebellar structures. The age-specific population-averaged-linear, population-averaged-nonlinear and single-subject templates were also generated. Incorporated with appropriate registration methods, high accuracy, high reproducibility, and low misclassification errors of automated labels using the established atlases were achieved. We also

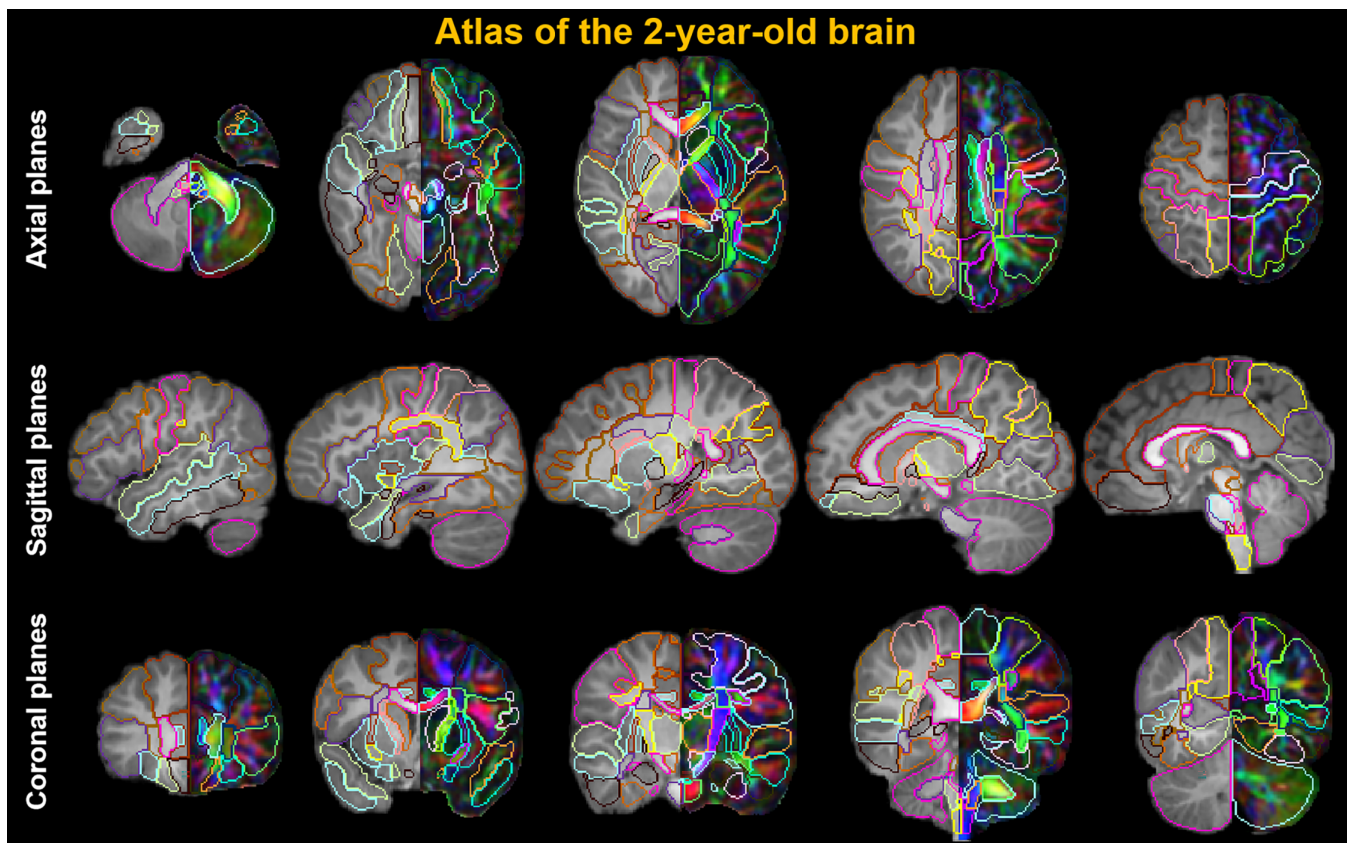


FIGURE 6 Axial, sagittal and coronal planes of the established 2-year-old brain atlas with comprehensive gray matter (GM) and white matter (WM) labels. Atlas labels are overlaid onto the T1w images (the left hemisphere) and DTI orientation-encoded colormaps (the right hemisphere) in axial and coronal planes. Atlas labels are overlaid onto the T1w images in sagittal planes.

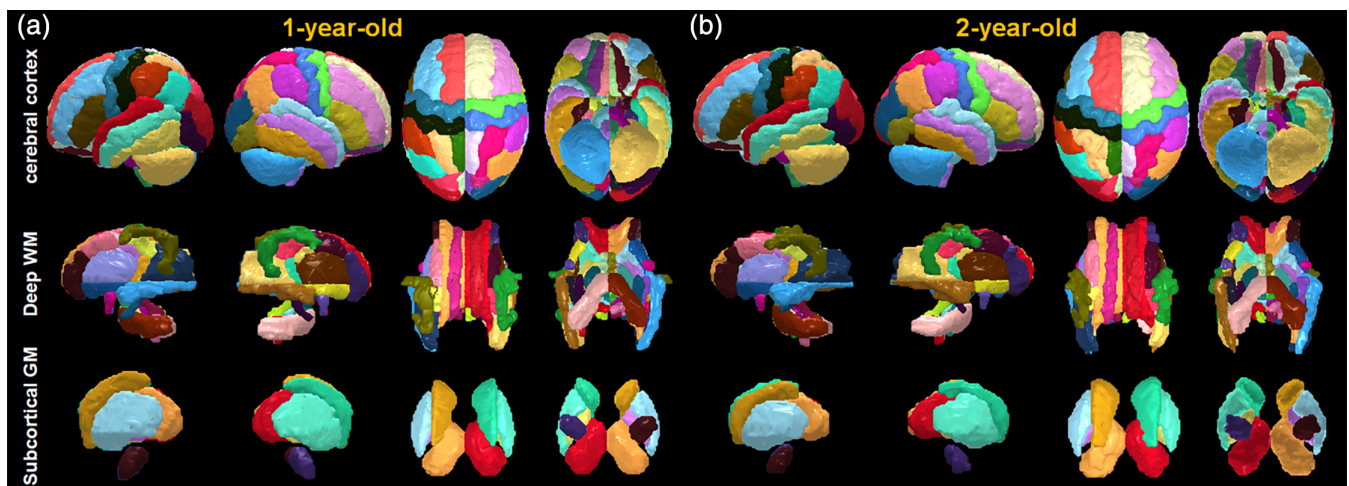


FIGURE 7 The three-dimensionally reconstructed labeled subcortical gray matter (GM) (bottom panels), deep white matter (WM) tracts (middle panels) and cerebral cortex (top panels) for 1-year-old (a) and 2-year-old (b) atlases. The lateral, superior, and inferior views of the 3D reconstructed labels are displayed from left to right for each panel.

demonstrated that using automated labels from age-specific atlases as ROIs can effectively reveal the heterogeneous WM microstructural maturation during the first 3 years of life. The established infant brain

atlases and templates can be applied to a broad range of analyses in brain health and diseases. These templates and atlases are freely available through the website www.brainmrmap.org.

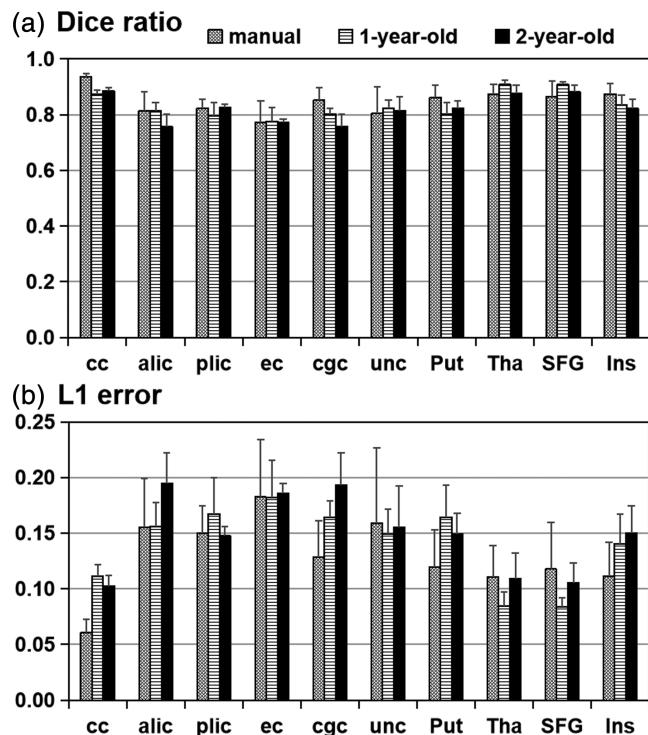


FIGURE 8 The Dice (a) and L1 error (b) measurements from the evaluation comparing automated labels with manual labels. The white bars with crossing lines, the white bars with horizontal lines, and the black bars in (a) and (b) show the Dice ratio and L1 error measures based on inter-rater (manual vs. manual delineations), automated labels of five children brains from 1-year-old atlas (manual vs. automated delineations), and automated labels of five toddler brains from 2-year-old atlas (manual vs. automated delineations) (see Table 1 for abbreviation of tested neural structures).

4.1 | Age-specific digital DTI brain templates and atlases for 1- and 2-year-old children brains

From birth to 2 years of age, the human brain structure changes rapidly and heterogeneously (Dubois et al., 2008; Dubois et al., 2016; Huang, 2022; Knickmeyer et al., 2008; Ouyang et al., 2019; Pfefferbaum et al., 1994). Notably, WM volume increases by around 11% in the first year and 19% in the second year, while GM volume expands by 106 and 18% during these respective periods (Knickmeyer et al., 2008; Ouyang, Smyser, et al., 2021). Meanwhile, WM microstructure also demonstrates differential maturation across major WM tracts and tract groups, with commissural tracts exhibiting the fastest development (Dubois et al., 2008; Ouyang et al., 2019; Yu et al., 2020). Due to the inhomogeneous change rates of GM and WM (Ouyang et al., 2019), the proportional size of each brain structure is dynamic during infancy. Using Jacobian determinates, we quantified local volume changes and identified relatively larger deformations in brains with bigger age differences from the templates during the registration process (Figure 2). We further observed that local volume changes were more prominent in the WM regions when registering infants' brain images to the adult template, consistent with previous

findings indicating WM growth contributes more to overall brain enlargement after age 2 (Knickmeyer et al., 2008; Ouyang, Smyser, et al., 2021). The significant and nonlinear difference between adult and pediatric brains underscores the importance of developing age-specific templates and atlases, especially during the first 2 years of life with dramatic and differential brain maturation. Using these age-appropriate templates and atlases is crucial to accurately characterizing local brain morphology and effectively alleviating automated labeling errors.

The brain templates created here for 1- and 2-year-old children include both DTI (e.g., b0, aDWI, FA and orientation-encoded color-map) and T1w contrasts (Figures 3 and 4), allowing us to conduct not only DTI-based studies (e.g., defining WM ROIs for microstructural analysis in Figure 9) but also structural MRI-based studies (e.g., defining nodes for brain network analysis). Each of these image contrasts can be used to drive registration during brain normalization. We created two types of population-averaged templates, representing the common brain features of 1- and 2-year-old infant populations, using linear and nonlinear transformations, respectively. The brain structures of these two templates appear smooth and slightly blurred, particularly in regions with high individual variability. The population-averaged-nonlinear template provides a sharper contrast for brain structures than the population-averaged-linear template. Depending on the study design, selecting the proper atlas sharpness and registration methods may improve brain normalization accuracy. In addition, we also created single-subject templates that preserve high sharpness of image contrast and clear boundaries of brain structures, promoting us to delineate the age-specific atlases.

Despite the growing interest in imaging the pediatric brain (e.g., Huang, 2022; Huang et al., 2019; Ouyang, Smyser, et al., 2021), as seen by landmark cohort studies such as the US Baby Connectome Project and Healthy Brain and Child Development (HBCD), atlases for the early developmental stages have not yet been well established (Oishi et al., 2019; Peng et al., 2020). Most existing atlases of 1- and 2-year-old children brains lack information about WM anatomy and often treat it as a uniform structure without any detailed anatomical annotations (e.g., Shi et al., 2011). Our age-specific DTI brain atlases, on the other hand, provide 124 comprehensive neuroanatomical labels, including the cerebral cortex and deep GM, as well as deep WM in the cerebrum, cerebellum, and brainstem (Figures 5–7). The various DTI images enabled us to identify brain structures and their locations (Figures 3 and 4), especially in WM regions, which conventional relaxation-based MRI (T1- or T2-weighted) struggles to differentiate due to poor image contrasts in the first 2 years of life. All major WM tracts can be easily identified and appreciated in these DTI maps, as shown in Figures 3–6. Although the manual delineation for establishing atlases was mainly performed on the axial planes, extensive adjustments and refinements by neuroanatomists (LS, LF) have been made in the coronal and sagittal planes to achieve naturally smooth boundaries of all brain structures in 3D. Given that many commonly used registration methods during brain normalization require image transformation in 3D, naturally smooth boundaries of brain structures in the atlases are crucial for later applications. Taken

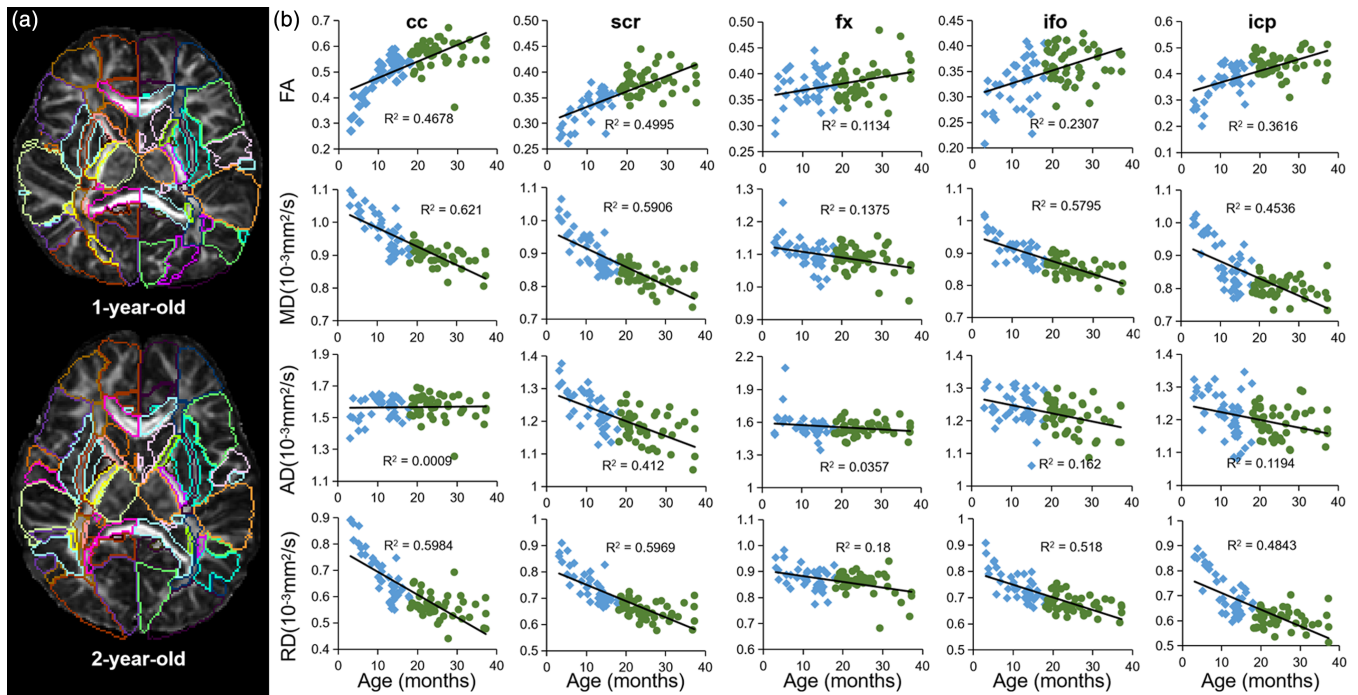


FIGURE 9 Application of the age-specific comprehensive atlases in exploring microstructural development of various white matter (WM) tracts. The registered 1- and 2-year-old parcellation maps were overlaid onto the representative FA images of a representative 1- and 2-year-old subject in native space in (a). The scatter plots of age-related FA, MD, AD, and RD changes of the five tracts representing the five WM tract groups in (b), including the commissural (cc), the projection (scr), the limbic (fx), the association (ifo), and the brainstem (icp) tract group. The blue diamonds represent the subjects aged 3–18 months, with their brain structures automatically labeled based on the 1-year-old atlas. The green circles represent the children aged 18–38 months, with their brain structures automatically labeled based on the 2-year-old atlas (see Table 1 for abbreviation of the WM tracts).

together, our established age-specific comprehensive DTI atlases, along with multi-contrast templates, can serve as standard references for brain functional and structural studies in these infant populations.

4.2 | Accuracy and evaluation of the automated labeling from the atlases

Defining ROIs based on neuroanatomy is crucial for quantifying the functional, structural, and physiological properties of various brain structures. Our established atlases can be used as 3D ROIs for qualitative studies on infant brain in health and disease. The atlas-based anatomical labeling approach enables the automatic and reproducible evaluation of brain structures, which is particularly beneficial for large-scale investigations (e.g., large sample size, large number of ROIs). To test the accuracy of this automated approach for delineating ROIs, we compared the automated labels from age-specific atlases with manual delineation using the Dice ratio and L1 error to evaluate the reliability and misclassification errors. The accuracy and reliability level of automated labeling was comparable to that of human raters. The averaged Dice ratio and L1 error of manual and atlas-based automated delineations for the 10 structures were 0.83 and 0.14, respectively, suggesting a high level of accuracy using atlas-based automated labeling (Figure 8). Dice ratios were slightly lower for brain

structures with irregular or thin shapes, such as cingulum in cingulate cortex (cgc) and external capsule (ec), but still exceeded 0.75, indicating substantial accuracy in the registration and labeling of all tested anatomical structures, including those difficult for labeling. It is worth mentioning that the accuracy of automated labeling depends on the quality of image registration between individual subjects and the age-specific template. If registration is poor, the atlas-based automated labeling would not align well with the subject's neural structures, affecting sequential quantitative analyses. Thus, visual inspection of registration quality is highly recommended when using the templates and atlases. Here, we used both affine and LDDMM transformations to transform the atlas parcellation maps into each subject's native space. Our 1- and 2-year-old infant atlases, when combined with proper registration procedures, can be applied to automatically and accurately delineate the brain structures of age-matched subjects.

4.3 | WM microstructural maturation during early childhood

To demonstrate the application of our age-specific atlases, we examined WM microstructural development during the first 3 years of life. Specifically, WM labels from the age-corresponding atlases were transformed into the subject brain (Figure 9a) to obtain the DTI-

derived microstructural measurements (e.g., FA, MD, AD, and RD) of the WM bundles across all five tract groups (Supplemental Table 1). Notably, the commissural tract group exhibits the highest averaged FA value, aligning with FA profiles seen in adults (e.g., Wakana et al., 2007) and children (e.g., Dubois et al., 2008; Ouyang et al., 2019; Yu et al., 2020). The order of WM tract groups with the smallest to largest averaged FA value is association tracts, limbic tracts, projection tracts, brainstem tracts, and commissural tracts in 1- and 2-year-old subjects (Supplemental Table 1). Moreover, the age-related changes in DTI metric measures of selected WM tracts for the first 3 years of life (Figure 9b) are consistent with earlier findings of WM maturation during the early developmental stages (e.g., Dubois et al., 2008; Ouyang et al., 2019; Yu et al., 2020). The commissural (cc) and limbic (fx) tracts displayed reduced RD and little AD changes, leading to increased FA and decreased MD, possibly due to ongoing myelination. Meanwhile, the projection (scr), association (ifo), and brainstem (icp) tracts showed decreased diffusivity measures and increased FA, suggesting a phase of membrane proliferation or “pre-myelination” in these fibers. In this example of using age-specific atlases, we employed linear regression to demonstrate age-related changes of WM microstructural measures. Noting that for specific tracts such as cc, the FA value trendline seems to follow a nonlinear pattern. The trajectory of WM microstructure development is dependent on the measurement used as well as the studied age range (Ouyang et al., 2019), and it is beyond the scope of this study to determine which model (e.g., linear, logarithmic, exponential, etc.) best fits the changes in DTI-derived measures of WM tracts during this developmental period.

4.4 | Potential research and clinical applications of the age-specific comprehensive atlases

Quantitative atlas-based image analysis plays an important role in monitoring normal brain development and detecting alterations in pathological conditions. There are several ways to use the presented age-specific atlases. First, it can be used to explore the different brain properties of various neural structures. One can wrap the digital labels from the atlas space to generate 3D ROIs in the individual's native image space, which allows for more straightforward volume and imaging measurement calculations of each parcellated anatomical structure. For example, we can delineate WM ROIs for microstructural measurements (e.g., Dubois et al., 2008; Ouyang et al., 2019), and cortical ROIs for macrostructural measurements such as cortical thickness (e.g., Wang et al., 2019), physiological measurements such as cerebral blood flow (e.g., Ouyang et al., 2017; Yu et al., 2023), or other quantitative parameters such as longitudinal relaxation time (T1) and transverse relaxation time (T2) (e.g., Leberberg et al., 2019). Given that the 1- and 2-year-old atlases cover the same brain regions as existing age-specific neonate atlases (e.g., Feng et al., 2019; Oishi et al., 2011), these infant and neonate atlases jointly can be potentially used in longitudinal studies such as the HBCD study (<https://hbcdstudy.org>) to investigate how

the same anatomical regions develop from age 0 to 3 years. In addition to directly quantifying brain properties, 3D ROIs from atlases can also serve as a basis for brain connection and topological investigation. For example, our age-specific atlases can be used to parcellate the cerebral cortex into nodes to explore the connectivity between different brain regions in functional (e.g., Cao et al., 2017; Gao et al., 2015; Smyser et al., 2010) and structural (e.g., Huang et al., 2015; Ouyang, Peng, et al., 2021) network research. Furthermore, our age-specific atlases will also aid clinical research in young children by identifying and categorizing brain disease-related changes into specific brain structures (e.g., autism in Ouyang et al., 2016). This allows us to pinpoint the most disease-sensitive regions, facilitating the development of imaging biomarkers for various brain disorders.

4.5 | Other technical considerations and limitations

Several technical considerations and limitations are elaborated below. Because population-averaged templates can blur anatomical details during averaging procedures, we conducted manual delineation of atlas labels on single-subject templates with clear and sharp brain structure boundaries. However, this approach has a potential drawback, as single-subject templates might be influenced by unique anatomical features specific to the selected participant. Using population-averaged templates for subsequent registration helps to mitigate this limitation. We combined cortical labels with associated superficial WM (SWM) to make our atlases more widely used. Due to more prominent intersubject anatomical differences at the cortical gyrus or SWM compared to the deep WM (DWM) regions (e.g., the labeled WM in our atlases), automated parcellation based on registration of atlas labels can relatively more accurately delineate DWM and deep GM (see, e.g., Figure 8), but not the boundaries between cortical gyri and SWM (Oishi et al., 2008). Integrating associated SWM into cortical labels results in less intersubject morphological variability of combined ROI than the cortical gyral ROI alone, imposing less challenges for automated labeling with intersubject registration. Such a labeling scheme has also been implemented in adult brain atlases, including the AAL (Tzourio-Mazoyer et al., 2002) and JHU brain atlases (Oishi et al., 2008; Oishi et al., 2011), which have been widely used in regional-wise studies, brain connection, and topological investigation. While our atlases label brain images effectively in age-matched normal infants, larger-scale validation is needed to assess their accuracy in cases involving brain disorders and patients with dramatically changed neuroanatomy. The number of participants in the 1- and 2-year-old age groups in our study is limited. Increasing the sample size within each age group in the future could capture a broader range of individual variances in the population-averaged templates. The DTI imaging resolution of all infants in the present study was $0.76 \times 0.76 \times 2 \text{ mm}^3$ (a nominal imaging resolution of isotropic 2 mm). Given the relatively small size of infant brains, the spatial resolution of DTI can be further improved to enhance the atlas labeling precision. With advances in MR techniques such as simultaneous

multiple-slice acquisition (Sotiropoulos et al., 2013), dMRI with higher spatial and angular resolutions could be potentially used for establishing atlases of infant brains delineating more anatomical details in the future.

5 | CONCLUSIONS

We established 3D age-specific atlases for 1- and 2-year-old human infant brains, parcellated into 124 regions using high-resolution T1w and DTI imaging data. The age-specific templates include population-averaged-linear, population-averaged-nonlinear, and single-subject templates. The evaluation based on Dice ratio and L1 error measurements suggested reliable and reproducible automated labels from the age-matched atlases compared to manual labeling. These age-specific atlases and templates are valuable for functional, structural, and connective analyses in infants, enhancing our understanding of early brain development, and serving as vital clinical anatomical references for the detection of neural abnormalities.

AUTHOR CONTRIBUTIONS

HH designed the research. LS, YP, MO, QP, LF, QY, HK, SL, and HH performed the research. LS, MO, QP, SS, KLS, and HH drafted and revised the paper. All authors discussed the results.

ACKNOWLEDGMENTS

This study is sponsored by National Institutes of Health (NIH R01MH092535, R01MH125333, R01EB031284, R01MH129981, R21MH123930, UM1MH130991, and P50HD105354); Natural Science Foundation of China (Grant Nos: 31571237 and 81671651 to S.L.); and Natural Science Foundation of Shandong Province (Grant No: ZR2020QH048 to L.S.).

CONFLICT OF INTEREST STATEMENT

The authors declare no conflict of interest.

DATA AVAILABILITY STATEMENT

The established 1-year-old and 2-year-old infant brain templates and atlases are available from the website www.brainmrimap.org, an openly available website maintained by the Huang lab.

ORCID

Yun Peng  <https://orcid.org/0000-0001-8213-9716>

Minhui Ouyang  <https://orcid.org/0000-0001-8013-2553>

Hao Huang  <https://orcid.org/0000-0002-9103-4382>

REFERENCES

- Alexander, B., Murray, A. L., Loh, W. Y., Matthews, L. G., Adamson, C., Beare, R., Chen, J., Kelly, C. E., Rees, S., Warfield, S. K., Anderson, P. J., Doyle, L. W., Spittle, A. J., Cheong, J. L. Y., Seal, M. L., & Thompson, D. K. (2017). A new neonatal cortical and subcortical brain atlas: The Melbourne Children's Regional Infant Brain (M-CRIB) atlas. *NeuroImage*, 147, 841–851.
- Barkovich, A. J. (2000). Concepts of myelin and myelination in neuroradiology. *AJNR. American Journal of Neuroradiology*, 21, 1099–1109.
- Basser, P. J., Mattiello, J., & LeBihan, D. (1994). MR diffusion tensor spectroscopy and imaging. *Biophysical Journal*, 66, 259–267.
- Cao, M., He, Y., Dai, Z., Liao, X., Jeon, T., Ouyang, M., Chalak, L., Bi, Y., Rollins, N., Dong, Q., & Huang, H. (2017). Early development of functional network segregation revealed by connectomic analysis of the preterm human brain. *Cerebral Cortex*, 27, 1949–1963.
- Collins, D. L., Neelin, P., Peters, T. M., & Evans, A. C. (1994). Automatic 3D intersubject registration of MR volumetric data in standardized Talairach space. *Journal of Computer Assisted Tomography*, 18, 192–205.
- Courchesne, E., & Pierce, K. (2005). Brain overgrowth in autism during a critical time in development: Implications for frontal pyramidal neuron and interneuron development and connectivity. *International Journal of Developmental Neuroscience*, 23, 153–170.
- de Macedo Rodrigues, K., Ben-Avi, E., Sliva, D. D., Choe, M. S., Drottar, M., Wang, R., Fischl, B., Grant, P. E., & Zollei, L. (2015). A FreeSurfer-compliant consistent manual segmentation of infant brains spanning the 0–2 year age range. *Frontiers in Human Neuroscience*, 9, 21.
- Desikan, R. S., Segonne, F., Fischl, B., Quinn, B. T., Dickerson, B. C., Blacker, D., Buckner, R. L., Dale, A. M., Maguire, R. P., Hyman, B. T., Albert, M. S., & Killiany, R. J. (2006). An automated labeling system for subdividing the human cerebral cortex on MRI scans into gyral based regions of interest. *NeuroImage*, 31, 968–980.
- Dubois, J., Dehaene-Lambertz, G., Perrin, M., Mangin, J. F., Cointepas, Y., Duchesnay, E., Le Bihan, D., & Hertz-Pannier, L. (2008). Asynchrony of the early maturation of white matter bundles in healthy infants: Quantitative landmarks revealed noninvasively by diffusion tensor imaging. *Human Brain Mapping*, 29, 14–27.
- Dubois, J., Poupon, C., Thirion, B., Simonnet, H., Kulikova, S., Leroy, F., Hertz-Pannier, L., & Dehaene-Lambertz, G. (2016). Exploring the early organization and maturation of linguistic pathways in the human infant brain. *Cerebral Cortex*, 26, 2283–2298.
- Fan, L., Li, H., Zhuo, J., Zhang, Y., Wang, J., Chen, L., Yang, Z., Chu, C., Xie, S., Laird, A. R., Fox, P. T., Eickhoff, S. B., Yu, C., & Jiang, T. (2016). The Human Brainnetome Atlas: A new brain atlas based on connective architecture. *Cerebral Cortex*, 26, 3508–3526.
- Feng, L., Jeon, T., Yu, Q., Ouyang, M., Peng, Q., Mishra, V., Pletikos, M., Sestan, N., Miller, M. I., Mori, S., Hsiao, S., Liu, S., & Huang, H. (2017). Population-averaged macaque brain atlas with high-resolution ex vivo DTI integrated into in vivo space. *Brain Structure & Function*, 222, 4131–4147.
- Feng, L., Li, H., Oishi, K., Mishra, V., Song, L., Peng, Q., Ouyang, M., Wang, J., Slinger, M., Jeon, T., Lee, L., Heyne, R., Chalak, L., Peng, Y., Liu, S., & Huang, H. (2019). Age-specific gray and white matter DTI atlas for human brain at 33, 36 and 39 postmenstrual weeks. *NeuroImage*, 185, 685–698.
- Gao, W., Alcauter, S., Elton, A., Hernandez-Castillo, C. R., Smith, J. K., Ramirez, J., & Lin, W. (2015). Functional network development during the first year: Relative sequence and socioeconomic correlations. *Cerebral Cortex*, 25, 2919–2928.
- Gilmore, J. H., Shi, F., Woolson, S. L., Knickmeyer, R. C., Short, S. J., Lin, W., Zhu, H., Hamer, R. M., Styner, M., & Shen, D. (2012). Longitudinal development of cortical and subcortical gray matter from birth to 2 years. *Cerebral Cortex*, 22, 2478–2485.
- Gousias, I. S., Edwards, A. D., Rutherford, M. A., Counsell, S. J., Hajnal, J. V., Rueckert, D., & Hammers, A. (2012). Magnetic resonance imaging of the newborn brain: Manual segmentation of labelled atlases in term-born and preterm infants. *NeuroImage*, 62, 1499–1509.
- Gousias, I. S., Rueckert, D., Heckemann, R. A., Dyet, L. E., Boardman, J. P., Edwards, A. D., & Hammers, A. (2008). Automatic segmentation of brain MRIs of 2-year-olds into 83 regions of interest. *NeuroImage*, 40, 672–684.
- Hazlett, H. C., Gu, H., Munsell, B. C., Kim, S. H., Styner, M., Wolff, J. J., Elison, J. T., Swanson, M. R., Zhu, H., Botteron, K. N., Collins, D. L.,

- Constantino, J. N., Dager, S. R., Estes, A. M., Evans, A. C., Fonov, V. S., Gerig, G., Kostopoulos, P., McKinsty, R. C., ... IBIS Network; Clinical Sites; Data Coordinating Center; Image Processing Core; Statistical Analysis. (2017). Early brain development in infants at high risk for autism spectrum disorder. *Nature*, *542*, 348–351.
- Herschkowitz, N. (2000). Neurological bases of behavioral development in infancy. *Brain Dev*, *22*, 411–416.
- Huang, H. (2022). Imaging the infant brain. In *Oxford research encyclopedia of psychology*. Oxford University Press.
- Huang, H., Huppi, P. S., He, Y., & Lerch, J. (2019). Imaging baby brain development. *NeuroImage*, *203*, 116142.
- Huang, H., Shu, N., Mishra, V., Jeon, T., Chalak, L., Wang, Z. J., Rollins, N., Gong, G., Cheng, H., Peng, Y., Dong, Q., & He, Y. (2015). Development of human brain structural networks through infancy and childhood. *Cerebral Cortex*, *25*, 1389–1404.
- Huang, H., Zhang, J., Jiang, H., Wakana, S., Poetscher, L., Miller, M. I., van Zijl, P. C., Hillis, A. E., Wytik, R., & Mori, S. (2005). DTI tractography based parcellation of white matter: Application to the mid-sagittal morphology of corpus callosum. *NeuroImage*, *26*, 195–205.
- Huang, H., Zhang, J., Wakana, S., Zhang, W., Ren, T., Richards, L. J., Yarowsky, P., Donohue, P., Graham, E., van Zijl, P. C., & Mori, S. (2006). White and gray matter development in human fetal, newborn and pediatric brains. *NeuroImage*, *33*, 27–38.
- Huppi, P. S., Warfield, S., Kikinis, R., Barnes, P. D., Zientara, G. P., Jolesz, F. A., Tsuji, M. K., & Volpe, J. J. (1998). Quantitative magnetic resonance imaging of brain development in premature and mature newborns. *Annals of Neurology*, *43*, 224–235.
- Jiang, H., van Zijl, P. C., Kim, J., Pearlson, G. D., & Mori, S. (2006). DtiStudio: Resource program for diffusion tensor computation and fiber bundle tracking. *Computer Methods and Programs in Biomedicine*, *81*, 106–116.
- Kabdebon, C., Leroy, F., Simmonet, H., Perrot, M., Dubois, J., & Dehaene-Lambertz, G. (2014). Anatomical correlations of the international 10–20 sensor placement system in infants. *NeuroImage*, *99*, 342–356.
- Knickmeyer, R. C., Gouttard, S., Kang, C., Evans, D., Wilber, K., Smith, J. K., Hamer, R. M., Lin, W., Gerig, G., & Gilmore, J. H. (2008). A structural MRI study of human brain development from birth to 2 years. *The Journal of Neuroscience*, *28*, 12176–12182.
- Lebenberg, J., Mangin, J. F., Thirion, B., Poupon, C., Hertz-Pannier, L., Leroy, F., Adibpour, P., Dehaene-Lambertz, G., & Dubois, J. (2019). Mapping the asynchrony of cortical maturation in the infant brain: A MRI multi-parametric clustering approach. *NeuroImage*, *185*, 641–653.
- Matsuzawa, J., Matsui, M., Konishi, T., Noguchi, K., Gur, R. C., Bilker, W., & Miyawaki, T. (2001). Age-related volumetric changes of brain gray and white matter in healthy infants and children. *Cerebral Cortex*, *11*, 335–342.
- Miller, M. I., Troune, A., & Younes, L. (2002). On the metrics and Euler-Lagrange equations of computational anatomy. *Annual Review of Biomedical Engineering*, *4*, 375–405.
- Mori, S., Crain, B. J., Chacko, V. P., & van Zijl, P. C. (1999). Three-dimensional tracking of axonal projections in the brain by magnetic resonance imaging. *Annals of Neurology*, *45*, 265–269.
- Mori, S., Oishi, K., Jiang, H., Jiang, L., Li, X., Akhter, K., Hua, K., Faria, A. V., Mahmood, A., Woods, R., Toga, A. W., Pike, G. B., Neto, P. R., Evans, A., Zhang, J., Huang, H., Miller, M. I., van Zijl, P., & Mazziotta, J. (2008). Stereotaxic white matter atlas based on diffusion tensor imaging in an ICBM template. *NeuroImage*, *40*, 570–582.
- Oishi, K., Chang, L., & Huang, H. (2019). Baby brain atlases. *NeuroImage*, *185*, 865–880.
- Oishi, K., Mori, S., Donohue, P. K., Ernst, T., Anderson, L., Buchthal, S., Faria, A., Jiang, H., Li, X., Miller, M. I., van Zijl, P. C., & Chang, L. (2011). Multi-contrast human neonatal brain atlas: Application to normal neonate development analysis. *NeuroImage*, *56*, 8–20.
- Oishi, K., Zilles, K., Amunts, K., Faria, A., Jiang, H., Li, X., Akhter, K., Hua, K., Woods, R., Toga, A. W., Pike, G. B., Rosa-Neto, P., Evans, A., Zhang, J., Huang, H., Miller, M. I., van Zijl, P. C., Mazziotta, J., & Mori, S. (2008). Human brain white matter atlas: Identification and assignment of common anatomical structures in superficial white matter. *NeuroImage*, *43*, 447–457.
- Ouyang, M., Cheng, H., Mishra, V., Gong, G., Mosconi, M. W., Sweeney, J., Peng, Y., & Huang, H. (2016). Atypical age-dependent effects of autism on white matter microstructure in children of 2–7 years. *Human Brain Mapping*, *37*, 819–832.
- Ouyang, M., Dubois, J., Yu, Q., Mukherjee, P., & Huang, H. (2019). Delineation of early brain development from fetuses to infants with diffusion MRI and beyond. *NeuroImage*, *185*, 836–850.
- Ouyang, M., Liu, P., Jeon, T., Chalak, L., Heyne, R., Rollins, N. K., Licht, D. J., Detre, J. A., Roberts, T. P. L., Lu, H., & Huang, H. (2017). Heterogeneous increases of regional cerebral blood flow during preterm brain development: Preliminary assessment with pseudo-continuous arterial spin labeled perfusion MRI. *NeuroImage*, *147*, 233–242.
- Ouyang, M., Peng, Q., Jeon, T., Heyne, R., Chalak, L., & Huang, H. (2020). Diffusion-MRI-based regional cortical microstructure at birth for predicting neurodevelopmental outcomes of 2-year-olds. *eLife*, *9*, e58116.
- Ouyang, M., Peng, Y., Sotardi, S., Hu, D., Zhu, T., Cheng, H., & Huang, H. (2021). Flattened structural network changes and association of hyperconnectivity with symptom severity in 2–7-year-old children with autism. *Frontiers in Neuroscience*, *15*, 757838.
- Ouyang, M., Smyser, C. D., Neil, J., & Huang, H. (2021). Chapter 19—Imaging early brain structural and functional development. In H. Huang & T. P. L. Roberts (Eds.), *Advances in magnetic resonance technology and applications* (pp. 395–428). Academic Press.
- Peng, Q., Ouyang, M., Wang, J., Yu, Q., Zhao, C., Slinger, M., Li, H., Fan, Y., Hong, B., & Huang, H. (2020). Regularized-Ncut: Robust and homogeneous functional parcellation of neonate and adult brain networks. *Artificial Intelligence in Medicine*, *106*, 101872.
- Pfefferbaum, A., Mathalon, D. H., Sullivan, E. V., Rawles, J. M., Zipursky, R. B., & Lim, K. O. (1994). A quantitative magnetic resonance imaging study of changes in brain morphology from infancy to late adulthood. *Archives of Neurology*, *51*, 874–887.
- Richards, J. E., & Xie, W. (2015). Brains for all the ages: Structural neurodevelopment in infants and children from a life-span perspective. *Advances in Child Development and Behavior*, *48*, 1–52.
- Shi, F., Yap, P. T., Wu, G., Jia, H., Gilmore, J. H., Lin, W., & Shen, D. (2011). Infant brain atlases from neonates to 1- and 2-year-olds. *PLoS One*, *6*, e18746.
- Smyser, C. D., Inder, T. E., Shimony, J. S., Hill, J. E., Degnan, A. J., Snyder, A. Z., & Neil, J. J. (2010). Longitudinal analysis of neural network development in preterm infants. *Cerebral Cortex*, *20*, 2852–2862.
- Sotiropoulos, S. N., Jbabdi, S., Xu, J., Andersson, J. L., Moeller, S., Auerbach, E. J., Glasser, M. F., Hernandez, M., Sapiro, G., Jenkinson, M., Feinberg, D. A., Yacoub, E., Lenglet, C., Van Essen, D. C., Ugurbil, K., Behrens, T. E., & WU-Minn HCP Consortium. (2013). Advances in diffusion MRI acquisition and processing in the Human Connectome Project. *NeuroImage*, *80*, 125–143.
- Toga, A. W., Thompson, P. M., Mori, S., Amunts, K., & Zilles, K. (2006). Towards multimodal atlases of the human brain. *Nature Reviews. Neuroscience*, *7*, 952–966.
- Tzourio-Mazoyer, N., Landeau, B., Papathanassiou, D., Crivello, F., Etard, O., Delcroix, N., Mazoyer, B., & Joliot, M. (2002). Automated anatomical labeling of activations in SPM using a macroscopic anatomical parcellation of the MNI MRI single-subject brain. *NeuroImage*, *15*(1), 273–289.
- Wakana, S., Caprihan, A., Panzenboeck, M. M., Fallon, J. H., Perry, M., Gollub, R. L., Hua, K., Zhang, J., Jiang, H., Dubey, P., Blitz, A., van Zijl, P., & Mori, S. (2007). Reproducibility of quantitative tractography methods applied to cerebral white matter. *NeuroImage*, *36*, 630–644.

- Wakana, S., Jiang, H., Nagae-Poetscher, L. M., van Zijl, P. C., & Mori, S. (2004). Fiber tract-based atlas of human white matter anatomy. *Radiology*, 230, 77–87.
- Wang, F., Lian, C., Wu, Z., Zhang, H., Li, T., Meng, Y., Wang, L., Lin, W., Shen, D., & Li, G. (2019). Developmental topography of cortical thickness during infancy. *Proceedings of the National Academy of Sciences of the United States of America*, 116, 15855–15860.
- Wilke, M., Schmithorst, V. J., & Holland, S. K. (2003). Normative pediatric brain data for spatial normalization and segmentation differs from standard adult data. *Magnetic Resonance in Medicine*, 50, 749–757.
- Woods, R. P., Grafton, S. T., Holmes, C. J., Cherry, S. R., & Mazziotta, J. C. (1998). Automated image registration: I. General methods and intra-subject, intramodality validation. *Journal of Computer Assisted Tomography*, 22, 139–152.
- Xu, D., Mori, S., Shen, D., van Zijl, P. C., & Davatzikos, C. (2003). Spatial normalization of diffusion tensor fields. *Magnetic Resonance in Medicine*, 50, 175–182.
- Yakovlev, P. I., & Lecours, A. (1967). *The myelogenetic cycles of regional maturation of the brain*. Blackwell Science.
- Yoshida, S., Oishi, K., Faria, A. V., & Mori, S. (2013). Diffusion tensor imaging of normal brain development. *Pediatric Radiology*, 43, 15–27.
- Yu, Q., Ouyang, M., Detre, J., Kang, H., Hu, D., Hong, B., Fang, F., Peng, Y., & Huang, H. (2023). Infant brain regional cerebral blood flow increases supporting emergence of the default-mode network. *eLife*, 12, e78397.
- Yu, Q., Peng, Y., Kang, H., Peng, Q., Ouyang, M., Slinger, M., Hu, D., Shou, H., Fang, F., & Huang, H. (2020). Differential white matter maturation from birth to 8 years of age. *Cerebral Cortex*, 30, 2673–2689.

SUPPORTING INFORMATION

Additional supporting information can be found online in the Supporting Information section at the end of this article.

How to cite this article: Song, L., Peng, Y., Ouyang, M., Peng, Q., Feng, L., Sotardi, S., Yu, Q., Kang, H., Sindabizera, K. L., Liu, S., & Huang, H. (2024). Diffusion-tensor-imaging 1-year-old and 2-year-old infant brain atlases with comprehensive gray and white matter labels. *Human Brain Mapping*, 45(7), e26695. <https://doi.org/10.1002/hbm.26695>